Physics – Uspekhi **64** (8) 836 – 851 (2021)

METHODOLOGICAL NOTES PACS numbers: 31.15.E –, 71.10.Ca, 71.15.Mb, **73.20. – r**

Two scales of quantum effects in a mesoscopic system of degenerate electrons

S E Kuratov, D S Shidlovski, S I Blinnikov, S Yu Igashov

DOI: https://doi.org/10.3367/UFNe.2020.08.038817

Contents

Abstract. A novel nontrivial manifestation of quantum effects in a spherical mesoscopic system of degenerate electrons (with $N_e \lesssim 10^9$ electrons) is demonstrated. Analysis shows that the electron distribution function has a large spatial scale, of the order of the system size, which is much greater than the other spatial scale, the Fermi length of the electron. This result is obtained following four different strategies: an analytic method of semiclassical Green's functions, direct numerical summation of the exact solutions for electron wave functions in an infinitely deep potential well, numerical construction of the exact Green's function using two linearly independent solutions, and the density functional method. The results obtained with these methods are in good qualitative and quantitative agreement with each other. We relate the nature of this phenomenon to quantum shell effects in a spherical mesoscopic system.

Keywords: electron distribution in a spherical potential, Green's function, density-functional theory, jellium model

S E Kuratov [1,*], **D S Shidlovski** [1,2], **S I Blinnikov** [1,2], **S Yu Igashov** [1]
[1] Dukhov Automatics Research Institute,
ul. Sushchevskaya 22, 127055 Moscow, Russian Federation
[2] National Research Center Kurchatov Institute,
Alikhanov Institute for Theoretical and Experimental Physics,
ul. Bol'shaya Cheremushkinskaya 25, 117218 Moscow,
Russian Federation
E-mail: [*] ser.evg.kuratov@gmail.com

Received 8 July 2020
Uspekhi Fizicheskikh Nauk **191** (8) 882 – 898 (2021)
Translated by S Alekseev

1. Introduction

This paper is devoted to a nontrivial manifestation of quantum effects in a spherical mesoscopic system of degenerate electrons. Specifically, we mean the appearance of a large scale in the spatial distribution of electrons.

The inhomogeneity of the spatial distribution of electrons in atoms is well known and well studied. In a spherically symmetric potential, the electron distribution density exhibits an oscillating behavior along the radius of the sphere. The spatial inhomogeneity scale is of the order of the atomic size. This is a general feature of electron density distributions and manifests itself in the results of calculations performed within different approaches: the Hartree–Fock and Hartree–Fock–Dirac methods, the Thomas–Fermi approximation [1–4], and the density functional theory (DFT) [5].

The oscillating behavior of the density is characteristic feature of not only the electron system but also systems of other particles with a more complicated interaction, e.g., in nuclear physics problems. In all such systems, the number of particles is relatively small ($N < 10^2$) and the inhomogeneity scale is of the order of several Fermi lengths.

In this paper, we show that the spatial distribution of a mesoscopic number ($N_e \lesssim 10^9$) of degenerate electrons also demonstrates an oscillating behavior, but with a spatial scale of the order of the system size. This scale can be much greater than the Fermi length of electrons λ_F.

We attribute the nature of this effect to quantum shell effects occurring in a spherical mesoscopic system similarly to such effects in metallic clusters. An example is provided by the oscillating behavior of specific energy as a function of the number of particles.

In this methodological note, we analyze this effect using four different approaches.

In Section 2, we outline two methods that allow to calculate numerically the concentration of a large number (up to $N_e \sim 10^9$) of degenerate electrons trapped in a spherical potential well with infinite walls.

In Section 2.1, we present an effective computational technique that allows to determine the electron density by numerical summation over the exact solutions, i.e., wave functions of free electrons in a potential well. In the framework of this approach, various systems with the number of electrons approaching $\sim 10^9$ have been studied. Such a large number of electrons N_e in the system has to be attained because it turns out, unexpectedly, that a homogeneous distribution does not simply set in, as was tacitly assumed in the limit of large N_e. The obtained results demonstrate the existence of a large inhomogeneity scale in the distribution of electrons.

In Section 2.2, we outline a numerical method for constructing an exact Green's function of the problem under study with the help of two linearly independent solutions. Using the determined Green's function, we calculate the concentration of electrons in the system. The results coincide with those obtained by numerical summation of the exact solutions for free-electron wave functions in Section 2.1.

An analytic treatment of the distribution of free electrons in a spherical potential well with the method of semiclassical Green's functions in Section 3 offers an insight into the cause of the inhomogeneity appearing in the system. Analysis shows that the spatial inhomogeneity scale is of the order of the radius of the potential well and can be several orders of magnitude greater than the distance between particles.

In Section 4, we present a numerical analysis of the inhomogeneous spatial distribution of electrons in a strongly pressurized deuterium gas bubble of submicrometer size. Characteristic values of the thermodynamical parameters pertaining to the pressurized gas are as follows: $\rho_{gas} \sim 10-30$ g cm^{-3}, $n_e \sim 10^{30-31}$ m^{-3}, $E_F \sim 20-100$ eV, and $T_i \sim T_e \sim 0.1-1$ eV (where T_i and T_e are the ion and electron temperatures, E_F is the Fermi energy, and ρ_{gas} is the gas density). All the electrons are free (the plasma is fully ionized) and degenerate, while the ions form a classical nonideal gas. The distribution of electrons was calculated numerically with the DFT method. We used the jellium model for hydrogen and sodium clusters (with the number of atoms in the model ranging from 8 to 400 thousand). The obtained results confirm the existence of a similar effect also in pressurized hydrogen gas bubbles.

2. Numerical methods

2.1 Direct summation of wave functions

2.1.1 Exact wave functions. A sufficiently simple model of a plasma bubble with up to $N_e = 10^9$ electrons is proposed. We consider a system of N_e electrons in the ground state in a spherically symmetric potential well of radius R_0 with impenetrable (i.e., infinitely high) walls,

$$V(r) = \begin{cases} 0\,, & r \leqslant R_0\,, \\ \infty\,, & r > R_0\,, \end{cases} \tag{1}$$

where r is the coordinate. This problem has an exact analytic solution; it was apparently for the first time studied by Gamow [6] and has long been included in textbooks (see, e.g., books [7] and [8]), already without references to the original source. We outline briefly the principal points of the solution. Due to the spherical symmetry, the Schrödinger equation enables the separation of variables, and its solutions can be written as

$$u(r,\theta,\varphi) = \frac{\chi(r)}{r}\, Y_{lm}(\theta,\varphi)\,, \tag{2}$$

where $Y_{lm}(\theta,\varphi)$ is a spherical harmonic [9]. The radial wave function $\chi(r)$ satisfies the equation

$$\left[\frac{\mathrm{d}^2}{\mathrm{d}r^2} - \frac{l(l+1)}{r^2} + k^2\right]\chi = 0\,, \quad k^2 = \frac{2mE}{\hbar^2}\,, \quad r \leqslant R_0\,. \tag{3}$$

The boundary condition

$$\chi(0) = 0 \tag{4}$$

follows from the boundedness of solution (2). The second boundary condition

$$\chi(R_0) = 0 \tag{5}$$

is related to the impenetrability of the walls. As a pair of linearly independent solutions of Eqn (3), we choose the Riccati–Bessel functions $z_1 j_l(z_1)$ and $z_1 y_l(z_1)$ (see [10]), where $z_1 = kr$, and j_l and y_l are spherical Bessel functions (see formulas (A.7) and (A.8) in the Appendix). The first boundary condition, Eqn (4), is satisfied automatically by the choice of the first solution in the form

$$\chi(r) = (kr)\, j_l\,(kr)\,. \tag{6}$$

The second boundary condition, Eqn (5), implies that

$$j_l\,(kR_0) = 0\,, \tag{7}$$

which results in the set of admissible values of k,

$$k_{n_r,l} = \frac{z_{n_r,l}}{R_0}\,, \tag{8}$$

where $z_{n_r,l}$ is the n_rth consecutive root of the spherical function $j_l(z)$. Below, the corresponding solutions and the related quantities are indexed in the similar manner, for example,

$$E_{n_r,l} = \frac{\hbar^2}{2m}\left(\frac{z_{n_r,l}}{R_0}\right)^2 \tag{9}$$

for the energy spectrum.

The normalized eigenfunctions

$$\chi_{n_r,l}(r) = C_{n_r,l}\, r\, j_l(k_{n_r,l}\, r)\,, \tag{10}$$

$$u_{n_r,lm}(r,\theta,\varphi) = C_{n_r,l}\, j_l(k_{n_r,l}\, r)\, Y_{lm}(\theta,\varphi) \tag{11}$$

are required to construct the Green's function by means of the spectral representation. The normalization constant $C_{n_r,l}$ can easily be found analytically, using the known result (see, e.g., [11]) for the indefinite integral:

$$\int x J_\nu^2(ax)\,\mathrm{d}x = \frac{x^2}{2}\left[J_\nu^2(ax) - J_{\nu-1}(ax) J_{\nu+1}(ax)\right] + \text{const}\,. \tag{12}$$

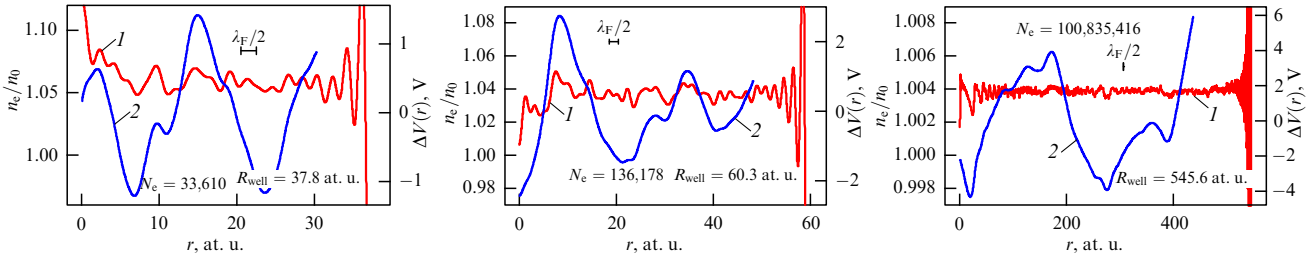

Figure 1. (Color online.) Oscillations of the electron density (red line *1*) and the electrostatic potential (blue line *2*) for three different numbers of electrons. Scale of half the Fermi length of the wave corresponding to the period of fast oscillations is shown in addition.

Because $z_{n_r,l}$ is a root of spherical Bessel function (A.7), we can find (cf. (A.28) in the Appendix)

$$C_{n_r,l}^{-2} = -\frac{R_0^3}{2}\, j_{l-1}(z_{n_r,l})\, j_{l+1}(z_{n_r,l})\,, \quad l \geqslant 1\,. \tag{13}$$

For $l = 0$, the normalization integral is especially simple, since $j_0(x) = \sin(x)/x$.

2.1.2 Expression for the density. We find the density by summing the squared moduli of normalized wave functions of occupied single-particle states (11). We assume that all the shells (labeled by a pair of quantum numbers n_r and l) are filled. This allows us to perform the summation over angular momentum projections analytically using the Unsöld theorem [9]:

$$\sum_{m=-l}^{l} \left|Y_{lm}(\theta,\varphi)\right|^2 = \frac{2l+1}{4\pi}\,. \tag{14}$$

The sum of contributions to the density of states is

$$\rho_s(r) = \frac{1}{4\pi r^2}\sum_{n_r,\,l}(2l+1)|\chi_{n_r,l}|^2\,. \tag{15}$$

With taking the spin states of the electron into account this result should be multiplied by the additional factor of 2. Thus, we obtain the following expression for the density of electrons n_e:

$$n_e(r) = \frac{2}{4\pi R_0^3}\sum_{n_r,\,l:\,E_{n_r,l}\leqslant E_F} 2(2l+1)\, j_l^2\left(\frac{z_{n_r,l}\, r}{R_0}\right) \times \left[-j_{l-1}(z_{n_r,l})\, j_{l+1}(z_{n_r,l})\right]^{-1}\,. \tag{16}$$

This implies, in particular, the self-similarity property: as the radius R_0 of the cavity changes, the density changes self-similarly as $f(x)/R_0^3$, where $x = r/R_0$.

2.1.3 Large scale of the spatial distribution of electrons. Results of the direct summation over states. In Fig. 1, red line *1* shows the results of calculations of the concentration of electrons for different numbers of electrons, performed with expression (16). The plot demonstrates an oscillatory behavior with a spatial scale of the order of the Fermi length. In order to demonstrate clearly the existence of the second spatial scale, we calculate the electrostatic potential arising in the system:

$$V(r) = 4\pi\left[\frac{1}{r}\int_0^r \rho_c(\bar r)\bar r^2\,\mathrm{d}\bar r + \int_r^{R_0}\rho_c(\bar r)\bar r\,\mathrm{d}\bar r\right]. \tag{17}$$

Here, $\rho_c = |e|(n_i - n_e)$ is the charge density, e is the elementary charge, and $n_e(r)$ is the density of electrons found from a calculation using formula (16); the simplest approximation of the homogeneous density

$$n_i(r) = \text{const} \tag{18}$$

is adopted for ions, small-scale oscillations are smoothed out by integration in (17) and the large scale manifests itself. Thus, the electrostatic potential calculation procedure plays the role of a filter with respect to small-scale oscillations.

We should note the following. In the model problem under consideration, electrostatic interaction between electrons and ions is not taken into account, and due to the boundary condition the electrons are displaced toward the center from the domain near the spherical well walls. This results in the essential excess of the mean concentration of electrons over the mean concentration of ions, and respectively an excess of negative charge emerges in the main domain. In order to eliminate a parabolic-profile potential arising in this case, we increase the mean density of ions to the mean density of electrons. Just that value is used in (18). Technically, this means that the constant in (18) is chosen from the condition of the minimal potential difference inside a sphere of radius R_0.

The results of calculations of the electrostatic potential are presented in Fig. 1 (and also in Fig. 10 below). These results demonstrate the existence of an inhomogeneity in the system and the appearance of a spatial scale of the order of the system size, which is much greater than the Fermi length. The behavior of the potential has the same character (with several extremum points) irrespective of the number of electrons and the value of the Fermi length $\sim h/p_F$.

The spatial distribution of electrons averaged over a scale greater than the Fermi length was calculated by means of averaging and smoothing procedures and depicted in Fig. 2. These results also demonstrate the existence of inhomogeneity in the system and the appearance of a spatial scale of the order of the system size, which is much greater than the Fermi length. The dependence of the density on the radius is similar to the dependence of the potential: several extremum points are detected.

Spherical symmetry of the system or closeness to this symmetry is of great importance for the effect. This can be shown with the example of the simplest problem of a one-dimensional electron gas in a potential well with infinitely high walls. The wave functions of electrons are

$$\Psi_k = \sqrt{\frac{2}{L}}\,\sin\frac{\pi k x}{L}\,, \quad E_k = \frac{\pi^2\hbar^2 k^2}{2m_e L^2}\,. \tag{19}$$

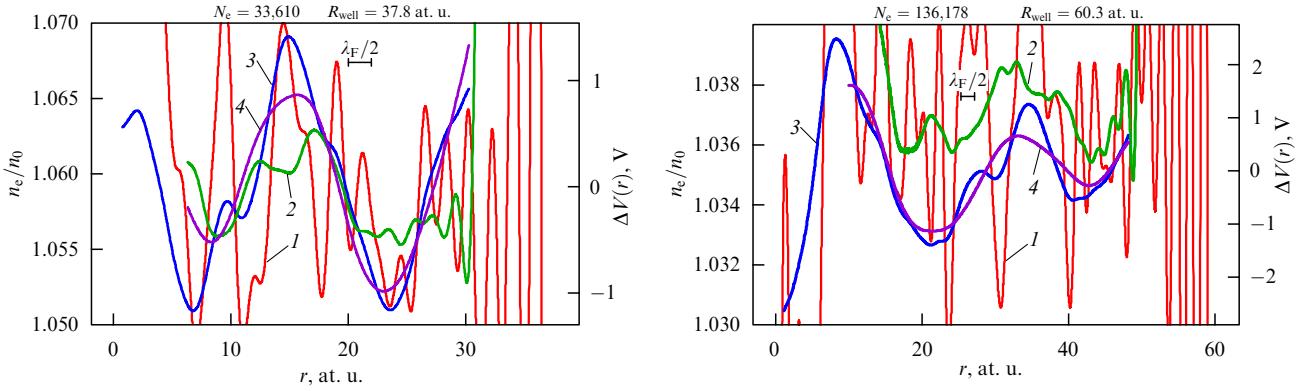

Figure 2. (Color online.) Original oscillations of the electron density for first two versions from Fig. 1 (thin red line *1*) on an enlarged scale, and highly smoothed density oscillations (thick green line *2*). Original electrostatic potential is shown by blue line *3* without changing the scale, and the smoothed electrostatic potential is shown by purple line *4*.

Accordingly, the concentration n_e is given by

$$n_e = \sum_1^{N_0} \Psi_k^2 = \sum_{k=1}^{N_0} \left(\sqrt{\frac{2}{L}} \sin \frac{\pi k x}{L} \right)^2 = \frac{1}{L} \sum_{k=1}^{N_0} \left(1 - \cos \frac{2\pi k x}{L} \right) = n_0 \left(1 + \frac{1}{N_0} - \frac{1}{N_0} \operatorname{cosec} \frac{\pi x}{L} \sin \frac{(N_0+1)\pi x}{L} \cos \frac{N_0 \pi x}{L} \right). \quad (20)$$

The final expression for the concentration $n_e \equiv N_0/L$ has two spatial scales. The first scale is the distance L/N_0 between particles (the factor $\sin((N_0+1)\pi x/L)\cos(N_0\pi x/L)$), which is essentially the Fermi length $\sim h/p_F$. The second scale is of the order of the system size L (the factor $\operatorname{cosec}(\pi x/L)$).

The behavior of the concentration of electrons determined by the large scale L has the following features. The concentration increases from zero to $n_e = n_0(1 + 1/N_0)$ in a small domain near the boundary, and remains constant in the main domain. Near this mean value, the concentration of electrons oscillates with a spatial scale of the order of the Fermi length of the electron (the factor $\sin((N_0+1)\pi x/L) \times \cos(N_0\pi x/L)$).

As shown above, in a spherically symmetric system, the behavior of the concentration of electrons averaged over a small scale is qualitatively different from the flat case. A similar behavior is observed near the boundary: an increase from zero to some mean value of the order of $n_e = n_0$. But the mean value of the concentration is not constant in the main domain: rather, it is of an oscillatory character, with a spatial scale of the order of the system size (see Fig. 2).

2.2 Numerical method for finding the concentration using the exact Green's function

2.2.1 Constructing the Green's function with the help of two linearly independent solutions. The Green's function of the Schrödinger equation is defined as a solution to the inhomogeneous equation

$$\left[-\frac{\hbar^2}{2m} \nabla^2 + V(r) - E \right] G(\mathbf{r}, \mathbf{r}', E) = \delta^{(3)}(\mathbf{r} - \mathbf{r}'), \quad (21)$$

satisfying the boundary conditions of the quantum mechanical problem under consideration. In the case of a spherically symmetric potential $V(r)$, the Green's function can be conveniently represented as a partial decomposition [12],

$$G(\mathbf{r}, \mathbf{r}', E) = -\frac{2m}{\hbar^2} \sum_{l=0}^{\infty} \sum_{m=-l}^{l} \frac{g_l(r, r', E)}{r r'} Y_{lm}^*(\mathbf{n}_{\mathbf{r}'}) Y_{lm}(\mathbf{n}_{\mathbf{r}}). \quad (22)$$

The common factor is chosen in (22) for convenience. Substituting this decomposition into (21) leads to an equation for partial Green's functions $g_l(r, r', k)$,

$$\left[\frac{\mathrm{d}^2}{\mathrm{d}r^2} - \frac{l(l+1)}{r^2} - v(r) + k^2 \right] g_l(r, r', k) = \delta(r - r'), \quad v(r) = \frac{2mV(r)}{\hbar^2}, \quad (23)$$

which has the form of an inhomogeneous radial Schrödinger equation. The relation between k and E is defined in (3). Knowing all the functions $g_l(r, r', k)$ is equivalent to ability to construct the full function $G(\mathbf{r}, \mathbf{r}', E)$. In most of the cases in quantum mechanical problems, restrictions occur for the orbital angular momenta involved, and therefore only a finite number of terms occur in decomposition (22).

In this paper, we use the model potential of an infinitely deep spherical potential well, Eqn (1). Requiring the solution of Eqn (21) to be bounded leads to the zero boundary condition at zero for the solution of radial equation (23). The other, also zero, boundary condition is imposed on the wall of the well.

The Green's function $g_l(r, r', k)$ being sought can be expressed in terms of two (linearly independent) solutions $\varphi_{1,2}(r)$ to homogeneous equation (3) that satisfy the respective boundary conditions (4) and (5):

$$\varphi_1(0) = 0, \quad (24)$$

$$\varphi_2(R_0) = 0. \quad (25)$$

The solutions $\varphi_1(r)$ and $\varphi_2(r)$ can be expressed through the already noted Riccati–Bessel functions

$$\varphi_1(r) = kr\, j_l(kr), \quad (26)$$

$$\varphi_2(r) = \alpha kr\, j_l(kr) + \beta kr\, y_l(kr). \quad (27)$$

The solution $\varphi_1(r)$ obviously satisfies condition (24). As regards the second solution $\varphi_2(r)$, satisfying condition (25)

requires that

$$\frac{\alpha}{\beta} = -\frac{y_l(kR_0)}{j_l(kR_0)}\,. \tag{28}$$

Following [12], we represent $g_l(r, r', k)$ as

$$g_l(r, r', k) = \frac{\varphi_1(r_<)\varphi_2(r_>)}{W_r[\varphi_1; \varphi_2]}\,, \tag{29}$$

where $r_< = \min(r, r')$, $r_> = \max(r, r')$, and $W_r[\varphi_1; \varphi_2]$ is the Wronskian of solution $\varphi_{1,2}(r)$:

$$W_r[\varphi_1; \varphi_2] = \varphi_1(r)\,\frac{\mathrm{d}\varphi_2(r)}{\mathrm{d}r} - \varphi_2(r)\,\frac{\mathrm{d}\varphi_1(r)}{\mathrm{d}r} = k\beta\,. \tag{30}$$

Relations (26)–(30) allow finding an explicit expression for $g_l(r, r', k)$:

$$g_l(r, r', k) = \frac{1}{k}\left[-\frac{y_l(kR_0)}{j_l(kR_0)}\,(kr)\,j_l(kr)(kr')\,j_l(kr') + (kr_<)\,j_l(kr_<)(kr_>)\,y_l(kr_>)\right]. \tag{31}$$

Expression (31) is used for numerical calculations in what follows.

2.2.2 Expressing density in terms of the Green's function. In the single-particle problem, when the fermions densely (without gaps) fill all the states up to E_F, it is relatively easy to evaluate the density of the spatial distribution of particles using the Green's function. The simplest case occurs for the problem with a purely discrete spectrum. As can be seen from the spectral representation of the Green's function

$$G(\mathbf{r}, \mathbf{r}', E) = -\sum_j \frac{u_j^*(\mathbf{r}')\,u_j(\mathbf{r})}{E - E_j}\,, \tag{32}$$

the integral of $G(\mathbf{r}, \mathbf{r}, E)$ in the complex plane of energy E along a closed contour that encompasses all poles corresponding to the filled states is equal to

$$-2\pi\mathrm{i}\sum_{j:\,E_j<E_\mathrm{F}} \left|u_j(\mathbf{r})\right|^2. \tag{33}$$

The multi-index j here includes all the quantum numbers labeling states (11). Thus, the numerical calculation of the density can be based on contour integration. Methodologically, it may be interesting to note that the representation (22) and (29) of the Green's function also allows arriving at this conclusion. Eigenfunctions satisfy two boundary conditions (24) and (25) simultaneously, which means the coincidence of solutions $\varphi_1(r)$ and $\varphi_2(r)$ and hence zeroing of the Wronskian in the denominator in (29), corresponding to a pole of $g_l(r, r', k)$ in the complex k plane. Let us consider the pole singularity of the Green's function in more detail for the example considered here, with the Green's function $g_l(r, r', k)$ having the relatively simple form (31). Heaving in mind the aim to calculate the spatial density by integrating along a complex-density contour encompassing some number of poles, it is sufficient to consider the pole term

$$g_l^{(\mathrm{pol})}(r, r', k) = -\frac{1}{k}\,\frac{y_l(kR_0)}{j_l(kR_0)}\,(kr)\,j_l(kr)(kr')\,j_l(kr')\,, \tag{34}$$

which does indeed make a contribution. The other term contains no singularities in the finite domain of the complex energy plane and does not contribute to the calculation of the contour integral. The poles in (34) are related to the roots $z_{n,l}$ of the spherical Bessel function $j_l(z)$. In the vicinity of some root $z_{n,l}$, restricting ourselves to the linear term, we can write

$$j_l(z) \approx j_l'(z_{n,l})(z - z_{n,l})\,, \tag{35}$$

which allows to find an approximate expression for (28) in the form

$$\frac{\alpha}{\beta} = -\frac{y_l(k_{n,l}R_0)}{j_l'(k_{n,l}R_0)(kR_0 - k_{n,l}R_0)}\,, \quad k_{n,l}R_0 \equiv z_{n,l}\,. \tag{36}$$

For further consideration it is advisable to transform expression (36) as follows. We first get rid of the numerator $y_l(k_{n,l}R_0)$ by expressing it through $j_l'(k_{n,l}R_0)$ using the known value of the Wronskian

$$W_z\left[j_l(z);\, y_l(z)\right] = j_l(z)\,y_l'(z) - j_l'(z)\,y_l(z) = \frac{1}{z^2} \tag{37}$$

and taking into account that $z_{n,l}$ is a root of $j_l(z)$. Next, we express the squared derivative $\left[j_l'(z_{n,l})\right]^2$ that then appears in the denominator in (36) in terms of the integral [11]

$$2\int_0^1 \left[x\,j_l(z_{n,l}x)\right]^2 \mathrm{d}x = \left[j_l'(z_{n,l})\right]^2, \tag{38}$$

which is a particular case of the more general Lommel-type integral

$$\int_0^x \zeta J_\nu^2(\lambda\zeta)\,\mathrm{d}\zeta = \frac{\lambda^2}{2}\left\{\left[J_\nu'(\lambda x)\right]^2 + \left(1 - \frac{\nu^2}{(\lambda x)^2}\right)\left[J_\nu(\lambda x)\right]^2\right\}. \tag{39}$$

As result of these transformations, we represent $g_l^{(\mathrm{pol})}(r, r', k)$ near the pole as

$$g_l^{(\mathrm{pol})}(r, r', k) \sim \frac{(k_{n,l}r)\,j_l(k_{n,l}r)(k_{n,l}r')\,j_l(k_{n,l}r')}{\int_0^{R_0}\left[(k_{n,l}\tilde{r})\,j_l(k_{n,l}\tilde{r})\right]^2\mathrm{d}\tilde{r}}\,\frac{1}{2k(k - k_{n,l})}\,. \tag{40}$$

The first factor in (40) is the product of normalized wave eigenfunctions of the problem. The denominator of the second factor can be rewritten as $2k(k - k_{n,l}) \approx (k + k_{n,l})\times(k - k_{n,l}) = k^2 - k_{n,l}^2$ for k in the close vicinity of $k_{n,l}$. As expected, the characteristics of the pole (its position and residue) coincide with those for the corresponding term in the spectral representation.

The aim of this analysis is not only to discuss the methodological aspect, which in this specific example allows clearly tracing the relation between the spectral representation of the Green's function and its representation with the use of two linearly independent solutions, but also to give a practical recipe for calculating the spatial density. We note once again that, in calculating the contour integral, it suffices to take only one of the pole terms (34) of the Green's function into account. We now briefly discuss some aspects relating to the method of calculation used in this paper. Integration in the complex energy plane can be transformed to integration in

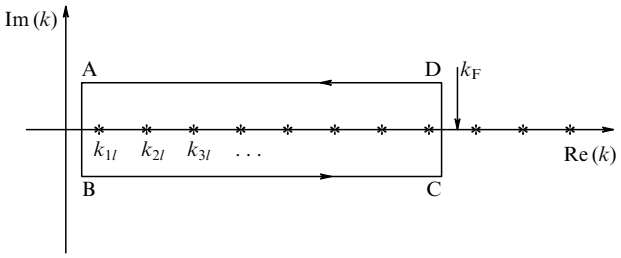

Figure 3. Integration contour.

the complex plane of the k variable, which is more convenient for performing numerical calculations.

One of possible choices of the integration contour is shown in Fig. 3. This contour, chosen as rectangle ABCD, encompasses a set of poles located to the left of k_F. In calculating the integral, it suffices to find only its imaginary part. If we choose segments AB and CD sufficiently short, then their contributions to the integral can be neglected. For the further simplification, we note that the values of the Green's function corresponding to complex-conjugate values of k are also complex conjugate. It then becomes clear that the imaginary parts of the integrals along segments BC and DA are the same. We can therefore restrict ourselves to integrating just the imaginary part of the Green's function along segment DA, which is assumed to be located sufficiently close to the real axis. These observations strongly reduce the number of calculations. Regarding the calculation of integrals of Green's function (34), we briefly note the methods for finding numerical values of the Bessel functions entering (34) with a small imaginary addition to the argument. Computations of the Bessel function $y_l(z)$ are usually not encounter difficulties. Recurrence relations are sufficiently effective and rather stable as l increases. Thus, starting with the values found from explicit expressions [10] for $l = 0$ and $l = 1$, we can calculate all the necessary values for larger l.

As for the function $j_l(z)$, its computations should be performed in the opposite direction. Asymptotic values of $j_l(z)$ for very large l can be used as the starting values. It is also rather convenient to use continued fractions. The values found can be corrected, for example, by comparing the $j_0(z)$ obtained within this approach with those evaluated directly from the explicit expression. Overall, these computation techniques allow calculating the Green's functions sufficiently effectively in the problem under consideration. Details of the algorithms for calculating Bessel functions can be found in [13, 14].

2.2.3 Results of calculations. Comparison of the approaches. The treatment in Section 2.2.2 allows us to formulate a sufficiently useful recipe for numerical calculations. The sum of squares of normalized radial wave functions (10) corresponding to states with an energy not exceeding E_F can be found in the form

$$s_l(r) \equiv \sum_{n_r:\, E_{n_r,l} \leqslant E_F} \left(\chi_{n_r,l}(r)\right)^2 = \frac{1}{2\pi} \operatorname{Im} \oint_{C_F} g_l^{(\mathrm{pol})}(r, r, k) 2k \, \mathrm{d}k$$
$$= \frac{-1}{\pi R_0} \operatorname{Im} \oint_{C_F} \frac{y_l(z)}{j_l(z)} \left[z\zeta j_l(z\zeta)\right]^2 \mathrm{d}z$$
$$= \frac{2}{\pi R_0} \operatorname{Im} \int_{0+\mathrm{i}\delta}^{z_F+\mathrm{i}\delta} \frac{y_l(z)}{j_l(z)} \left[z\zeta j_l(z\zeta)\right]^2 \mathrm{d}z \,, \qquad (41)$$

where $z = kR_0$, $z_F = k_F R_0$, and $\zeta = r/R_0$. The spatial density of states is found by summing the partial contributions (see (15))

$$\rho_s(r) = \frac{1}{4\pi r^2} \sum_l (2l+1)\, s_l(r) = \sum_l (2l+1)\, \rho_l(r) \,, \qquad (42)$$

where

$$\rho_l(r) = \frac{1}{2\pi^2 R_0^3} \operatorname{Im} \int_{0+\mathrm{i}\delta}^{z_F+\mathrm{i}\delta} \frac{y_l(z)}{j_l(z)} \left[z j_l(z\zeta)\right]^2 \mathrm{d}z \,. \qquad (43)$$

Applying the theory of residues to integral (43), it is easy to verify that it leads to the expression for density in Eqn (16), obtained by direct summation of wave functions, without any knowledge that this integral was obtained from the Green's function of the system.

The electron densities of states for two systems were calculated in the framework of the above method, with the results presented in Fig. 4. There, we also show the results

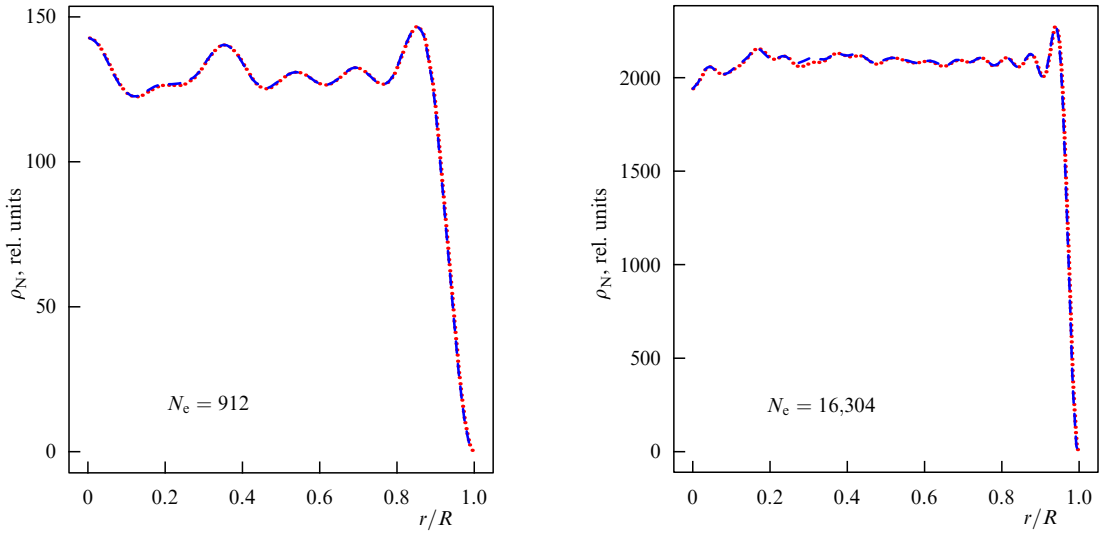

Figure 4. (Color online.) Distribution of the density of states of electrons obtained by two numerical methods. Red: formulas in Section 2.1.2; blue: formulas in Section 2.2.2.

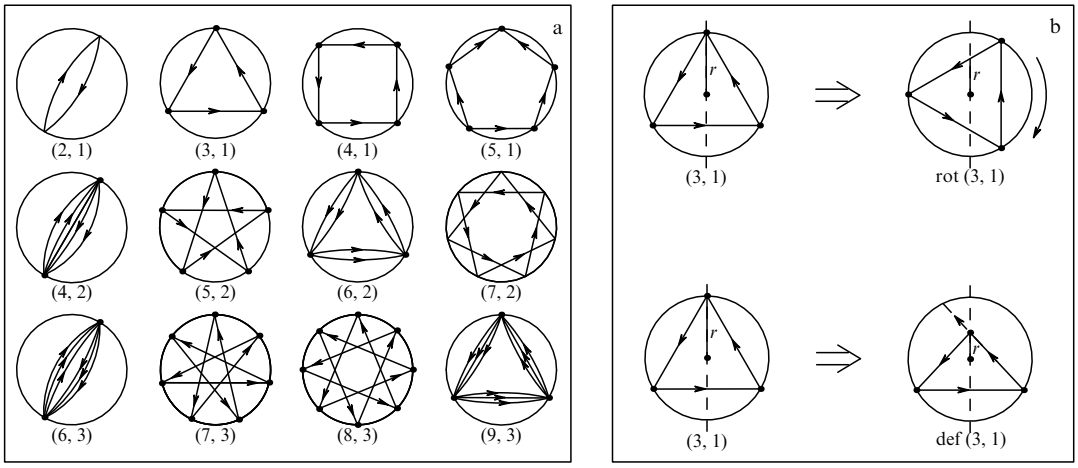

Figure 5. (a) Periodic trajectories of an electron. (b) Formation of two trajectory types.

of similar calculations performed by direct summation of the wave functions (see Section 2.1). The results are practically coincident. This indicates the high accuracy of the proposed numerical techniques for computing the concentration of electrons.

3. Analytic method. Method of semiclassical Green's functions

We use the method of Green's functions to analyze the distribution of free degenerate electrons in a spherical potential well with infinitely high walls. The electron states are characterized by rather large orbital angular momenta and are therefore semiclassical. This allows using the semiclassical approximation in the theoretical analysis. This way allows understanding the underlying cause of the appearance of inhomogeneity in the system and obtaining analytic dependences of the distribution of electrons on the system parameters. The semiclassical approach is widely used for the analysis of metallic clusters [2], for calculating the energy spectrum of nuclei [15], and for calculating oscillations of the electron concentration in an atom [4].

3.1 General relations

To find the electron concentration, we use the representation of the Green's function $G(\mathbf{r}'', \mathbf{r}', E)$ for electrons within the semiclassical approximation [15–19], where $\mathbf{r}'$ and $\mathbf{r}''$ are the respective initial and final points of the trajectory, and E is the energy:

$$G(\mathbf{r}'', \mathbf{r}', E) = G_0 - \frac{1}{(2\pi h^5)^{1/2}} \times \sum_{\alpha} \left\{ p_\rho D^{1/2} \exp\left(\frac{\mathrm{i}}{h} S_\alpha(\mathbf{r}'', \mathbf{r}', E) - \frac{\mathrm{i}\pi}{4} \right) \right\}_\alpha , \tag{44}$$

where S_α is the classical action integral:

$$S_\alpha = \int_{\mathbf{r}'}^{\mathbf{r}''} p_\alpha \, \mathrm{d}l_\alpha , \tag{45}$$

$$G_0(\mathbf{r}'', \mathbf{r}', E) = -\frac{m}{2\pi h^2 |\mathbf{r}'' - \mathbf{r}'|} \exp\left(\frac{\mathrm{i}}{h} |\mathbf{r}'' - \mathbf{r}'| \, p(\mathbf{r}) \right) , \tag{46}$$

$$\mathbf{r} = \frac{\mathbf{r}' + \mathbf{r}''}{2} , \quad \mathbf{p}' = \frac{\mathrm{d}S_\alpha(\mathbf{r}', \mathbf{r}'', E)}{\mathrm{d}\mathbf{r}'} , \quad \mathbf{p}'' = \frac{\mathrm{d}S_\alpha(\mathbf{r}', \mathbf{r}'', E)}{\mathrm{d}\mathbf{r}''} . \tag{47}$$

To evaluate $G(\mathbf{r}'', \mathbf{r}', E)$, it is more convenient to use a cylindrical coordinate system $(\rho z \varphi)$, where the z-axis is directed along $(0, \mathbf{r})$, the point $\mathbf{r}$ being the center. The momentum components p_ρ and p_z and the angle φ_p are then expressed as $p_\rho = (p_x^2 + p_y^2)^{1/2}$, p_z, and $\varphi_p = \arctan(p_y/p_x)$:

$$D = \det \begin{bmatrix} \dfrac{\mathrm{d}p'_\rho}{\mathrm{d}\rho''} & \dfrac{\mathrm{d}p'_\rho}{\mathrm{d}z''} & \dfrac{\mathrm{d}p'_\rho}{\mathrm{d}E''} \\ \dfrac{\mathrm{d}p'_z}{\mathrm{d}\rho''} & \dfrac{\mathrm{d}p'_z}{\mathrm{d}z''} & \dfrac{\mathrm{d}p'_z}{\mathrm{d}E''} \\ \dfrac{\mathrm{d}t_\alpha}{\mathrm{d}\rho''} & \dfrac{\mathrm{d}t_\alpha}{\mathrm{d}z''} & 0 \end{bmatrix} , \tag{48}$$

$$t_\alpha(\mathbf{r}', \mathbf{r}'') = \frac{\mathrm{d}S_\alpha(\mathbf{r}', \mathbf{r}'', E)}{\mathrm{d}E} = \int_{\mathbf{r}'}^{\mathbf{r}''} \frac{1}{|\dot{\mathbf{r}}|} \, \mathrm{d}l_\alpha . \tag{49}$$

The summation in (44) is performed over all real classical trajectories α that connect points with the coordinates $\mathbf{r}'$ and $\mathbf{r}''$, and t_α is the time of motion along α.

The electron concentration is determined by the following expression, which includes the imaginary part of the Green's function:

$$n_\mathrm{e}(r) = -\frac{2}{\pi} \int_{-\infty}^{E_\mathrm{F}} \mathrm{Im}\left\{ G(r, r, E) \right\} \mathrm{d}E . \tag{50}$$

In our case, the calculation of electron density (50) consists in taking into account all orbits with coincident initial and finite points.

All of the closed electron orbits starting and terminating at $\mathbf{r}$ belong to one of two types: closed periodic and closed nonperiodic. The classification of all such closed (periodic and nonperiodic) orbits adopted here is based on the well-known (n, m) classification of closed periodic orbits, where n is the number of turning points and m is the number of turns of the trajectory around the center. Closed nonperiodic orbits can be formed from periodic ones by a single transformation, which is a shift of one of the vertices to the point $\mathbf{r}$, i.e., by a deformation of a periodic (n, m) orbit. We therefore label them def (n, m). Closed periodic orbits are just the known periodic (n, m) orbits that goes through the point $\mathbf{r}$. Depending on $\mathbf{r}$, the orbit can be oriented differently in the plane of the drawing. As $\mathbf{r}$ varies, the periodic (n, m) orbit rotates in the plane of the drawing, and we therefore use the notation rot (n, m) for such orbits.

Examples of trajectories of both types are presented in Fig. 5. These trajectories, as noted above, can be formed from the known periodic orbits (Fig. 5a) in two ways: by rotation or deformation (Fig. 5b).

Closed periodic trajectories occur more frequently in the literature because they alone are used to calculate the energy spectrum of the system. However, our study is devoted to the spatial distribution of electrons. This requires to take into consideration both types of trajectories in calculations, as noted, for example, in [18, p. 1797], where it was stated that the spectrum is determined only by periodic orbits, despite the wave functions being made of **both types** of trajectories.

The general expression for the contribution of each trajectory to the concentration n in (50) is

$$S_\alpha \sim pR_0 L_\alpha\left(\frac{\mathbf{r}'}{R_0}, \frac{\mathbf{r}''}{R_0}\right) = pR_0 L_\alpha(\mathbf{x}', \mathbf{x}''), \tag{51}$$

where L_α is a dimensionless length of the trajectory α and R_0 is the radius of the well. Here and hereafter, the notation $\mathbf{x} = \mathbf{r}/R_0$ is adopted. We define a dimensionless function F_α as follows:

$$p_\rho D_\alpha^{1/2} = \frac{m\sqrt{p}}{\sqrt{R_0}} F_\alpha(\mathbf{x}', \mathbf{x}''). \tag{52}$$

The second term of the right-hand side of expression (44) for the Green's function can be represented as

$$\Delta G(\mathbf{r}'', \mathbf{r}', E) = \frac{1}{h^{5/2}} p\left(\frac{m^2}{R_0 p}\right)^{1/2} \times F_\alpha(\mathbf{x}', \mathbf{x}'') \exp\left(\frac{\mathrm{i}}{h} pR_0 L_\alpha(\mathbf{x}', \mathbf{x}'')\right). \tag{53}$$

The imaginary part of $\Delta G(\ldots)$ determines the difference between concentrations $n(r)$ and n_0:

$$n(r) - n_0 = \Delta n(r) = -\frac{2}{\pi}\int_{-\infty}^{E_\mathrm{F}} \mathrm{Im}\left\{\Delta G(r, r, E)\right\} \mathrm{d}E. \tag{54}$$

Since the density of electrons is expressed through the Green's function with $\mathbf{r}' = \mathbf{r}''$ and depends only on $r = |\mathbf{r}|$ in the spherically symmetric case, we use r instead of $\mathbf{r}$, as an argument of G in (50) and (54). Correspondingly, the notation $x = |\mathbf{r}|/R_0$, rather than $\mathbf{x}$, is used in the functions F_α and L_α below.

To calculate the integral in (54), we assume a large ($\sim 10^3$) absolute value of the exponential in (53). As a result, we obtain the expression

$$\frac{\Delta n(r)}{n_0} = \sum_\alpha \frac{F_\alpha(x, x)}{L_\alpha(x, x)} \left(\frac{8}{N}\right)^{1/2} \sin\left[\frac{1}{h} p_\mathrm{F} R_0 L_\alpha(x, x)\right]. \tag{55}$$

The contribution of each trajectory to (55) is taken into account additively. Several corollaries follow from expression (55).

The dependence of the relative deviation of the concentration on the number of particles has the form

$$\left(\frac{\Delta n}{n_0}\right)_\mathrm{sphere} \sim \sqrt{\frac{8}{N}}. \tag{56}$$

Expression (55) contains two spatial scales. The first of them is the Fermi length $\sim h/p_\mathrm{F}$ and the second one is the size R_0 of the potential well. The spatial dependence in (55) has a qualitatively different nature for two types of trajectories, rot (n, m) and def (n, m).

For rot (n, m) trajectories, the spatial dependence of each term in (55) is determined by the factor F_α only, because L_α is independent of x. Therefore, the total contribution to (55) from trajectories of this type forms a function that has a spatial inhomogeneity scale of the order of R_0 only. For def (n, m) trajectories, each term in the sum is the product of a rapidly oscillating function $\sin\left[p_\mathrm{F} R_0 L_\alpha(x, x)/h\right]$ with the spatial inhomogeneity scale $\sim h/p_\mathrm{F}$ and a slowly varying function $F_\alpha(x, x)/L_\alpha(x, x)$ with the spatial scale $\sim R_0$. Therefore, the spatial dependence of the relative deviation of concentration consists of a rapidly oscillating part (Fermi length scale) and a slowly oscillating part (scale of the system size):

$$\left(\frac{\Delta n}{n_0}\right)_\mathrm{sphere} = \left(\frac{\Delta n}{n_0}\right)_\mathrm{FOscil} + \left(\frac{\Delta n}{n_0}\right)_\mathrm{SOscil}. \tag{57}$$

The former part is defined by the sum in (55) over def (n, m)-type trajectories, and the latter part is defined by the sum in (55) over rot (n, m)-type trajectories.

Each term in (55) is proportional to $1/L_\alpha$ and decreases as m increases, because $L_\alpha \sim m$. Therefore, the sum is determined by terms with small m, i.e., the trajectories def $(n, 1)$ and rot $(n, 1)$.

3.2 Examples of diagram calculations

As was shown in Section 3.1, the expression for the concentration of electrons is determined by closed trajectories and is given by (55).

In this section, we show the main properties of the functions $F_\alpha(x, x)$ and $L_\alpha(x, x)$ with the example of def $(3, 1)$, def $(4, 1)$, rot $(3, 1)$, and rot $(4, 1)$ trajectories, for which analytic expressions can be found in a closed form. These results suggest general conclusions regarding the structure of F_α and the nature of the spatial distribution of electrons. In addition, these trajectories make the leading contribution to the respective sums in (76) and (75) (see Section 3.3 in what follows), because they correspond to small values of m. Search for $F_\alpha(x, x)$ turns into calculating the determinant at $\mathbf{r}' = \mathbf{r}''$. The closeness of $\mathbf{r}'$ and $\mathbf{r}''$ to each other simplifies the calculation.

Let us describe the calculation for the def $(3, 1)$ trajectory in detail. Figure 6 demonstrates a closed nonperiodic def $(3, 1)$ trajectory together with a nearby nonclosed trajectory (shown in red) whose initial and final positions $\mathbf{r}'$ and $\mathbf{r}''$ are close, but distinct. In a Cartesian coordinate system (x, y), we introduce the notations $(\rho' z')$ and $(\rho'' z'')$ for components of these vectors.

The following relations hold:

$$\frac{\sin\alpha}{r} = \frac{\cos 2\alpha}{R_0}, \qquad \frac{\sin(\alpha + \varepsilon)}{r + \Delta} = \frac{\cos(2\alpha + 2\varepsilon)}{R_0}. \tag{58}$$

Because $\mathbf{r}'$ and $\mathbf{r}''$ are close, the parameters ε and Δ have small values, and therefore

$$\varepsilon\left(\frac{\cos\alpha}{r} + \frac{2\sin 2\alpha}{R_0}\right) = \frac{\Delta \sin\alpha}{r^2}, \tag{59}$$

$$\Delta = \frac{1}{2r(R_0 \sin\alpha + r)}\left[\left(-\frac{r^2 \sec\alpha}{R_0} - r\tan\alpha\right)(-R_0\rho' \sin\alpha - R_0\rho'' \sin\alpha + R_0 z' \cos\alpha - R_0 z'' \cos\alpha - r\rho' - r\rho'')\right] - \frac{r\rho' \sec\alpha + R_0\rho' \tan\alpha - R_0 z'}{R_0}, \tag{60}$$

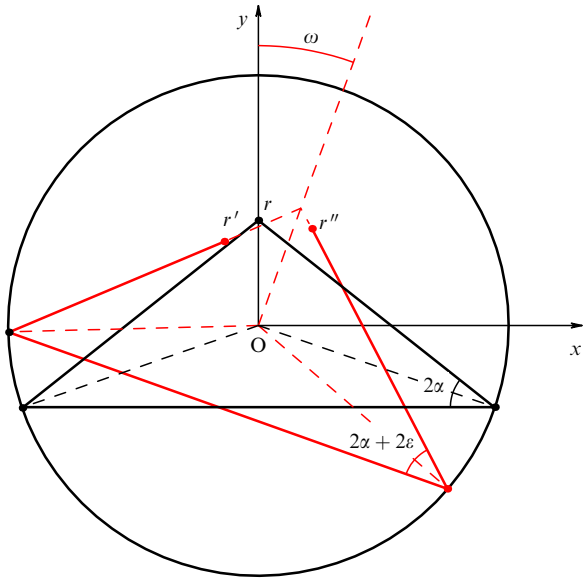

Figure 6. def (3, 1) electron trajectories.

$$\omega = \frac{1}{2r(R_0 \sin\alpha + r)}\Big(- R_0\rho' \sin\alpha - R_0\rho'' \sin\alpha + R_0 z' \cos\alpha - R_0 z'' \cos\alpha - r\rho' - r\rho''\Big)\,, \tag{61}$$

$$p_\rho = p(2\varepsilon \sin 2\alpha - 2\omega \sin 2\alpha - \cos 2\alpha)\,, \tag{62}$$

$$p_z = p(-2\varepsilon \cos 2\alpha + 2\omega \cos 2\alpha - \sin 2\alpha)\,. \tag{63}$$

Substituting the obtained expression in (48) and also tending $\mathbf{r}'$ and $\mathbf{r}''$ to $\mathbf{r}$, we find

$$F_{\mathrm{def}\,(3,1)}(x,x) = \frac{-1+\sqrt{8x^2+1}}{4x^2} \times \sqrt{\frac{8x^3\big(4x^2+5+3\sqrt{8x^2+1}\big)}{\sqrt{8x^2+1}\big(4x^2-1+\sqrt{8x^2+1}\big)^{5/2}\sqrt{4x^2+1+\sqrt{8x^2+1}}}} \quad \text{for} \quad x \geqslant 0\,, \tag{64}$$

$$L_{\mathrm{def}\,(3,1)}(x,x) = 4\,\frac{\cos^3\alpha}{\cos 2\alpha}\,, \qquad \sin\alpha = \frac{-1/2+\sqrt{1/4+2x^2}}{2x}\,, \quad 0 < x < 1\,. \tag{65}$$

Similar calculations yield closed analytic expressions for the def (4, 1) trajectories (Fig. 7):

$$F_{\mathrm{def}\,(4,1)}(x,x) = \begin{cases} \sqrt{\dfrac{\sqrt{x/\big[(1-2x)^2(1+x)\big]}}{(3x-1)}}\,\sin\left[3\arccos\dfrac{1}{2}\sqrt{1+\dfrac{1}{x}}\right] & \text{for} \quad x \geqslant \dfrac{1}{3}\,, \\ 0 & \text{for} \quad x < \dfrac{1}{3}\,, \end{cases} \tag{66}$$

$$L_{\mathrm{def}\,(4,1)}(x,x) = 2\sin 2\alpha\left(\frac{1}{\sin 3\alpha}+\frac{1}{\sin\alpha}\right)\,, \qquad x = \frac{\sin\alpha}{\sin 3\alpha}\,, \quad 0 < x < 1\,. \tag{67}$$

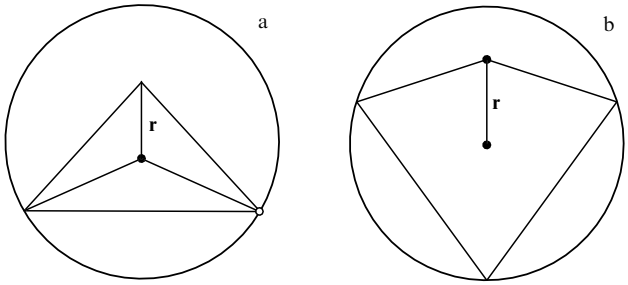

Figure 7. (a) def (3, 1) and (b) def (4, 1) electron trajectories.

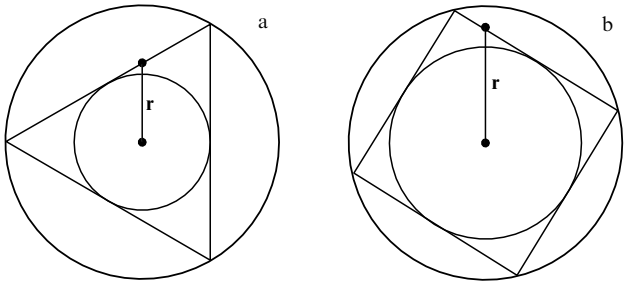

Figure 8. (a) rot (3, 1) and (b) rot (4, 1)(*b*) electron trajectories.

For rot-type trajectories (Fig. 8), we have

$$F_{\mathrm{rot}\,(3,1)}(x,x) = \begin{cases} -\dfrac{1}{2x}\sqrt{\dfrac{1}{\sqrt{3}(4x^2-1)}} & \text{for} \quad x \geqslant \dfrac{1}{2}\,, \\ 0 & \text{for} \quad x < \dfrac{1}{2}\,, \end{cases} \tag{68}$$

$$L_{\mathrm{rot}\,(3,1)}(x,x) = 3\sqrt{3}\,, \tag{69}$$

$$F_{\mathrm{rot}\,(4,1)}(x,x) = \begin{cases} \dfrac{1}{4\sqrt{2}(2x^2-1)} & \text{for} \quad x \geqslant \dfrac{\sqrt{2}}{2}\,, \\ 0 & \text{for} \quad x < \dfrac{\sqrt{2}}{2}\,, \end{cases} \tag{70}$$

$$L_{\mathrm{rot}\,(4,1)}(x,x) = 4\sqrt{2}\,. \tag{71}$$

Now it is clear that the nonoscillating part of the sum in (55) is associated with the terms where L_α is constant. Accordingly, the oscillating one is the part of (55) where L_α is variable.

Several important properties follow from the obtained expressions.

(1) The function F_α is nonvanishing for $r > s_\alpha$:

(a) $s_{\mathrm{rot}\,(n,1)} = R_0 \sin\dfrac{(n-2)\pi}{2n}$;

(b) $s_{\mathrm{def}\,(n,1)} \cong s_{\mathrm{rot}\,(n-1,1)}$.

(2) The function F_α is singular at the points d_α:

(a) $d_{\mathrm{rot}\,(n,1)} = s_{\mathrm{rot}\,(n,1)}$;

(b) $d_{\mathrm{def}\,(n,1)} = s_{\mathrm{rot}\,(n-1,1)}$.

Thus, F_α can be represented as

$$F_\alpha(x,x) = \Theta(r-s_\alpha)G_\alpha\left(x,\frac{r}{s_\alpha}\right)\,, \tag{72}$$

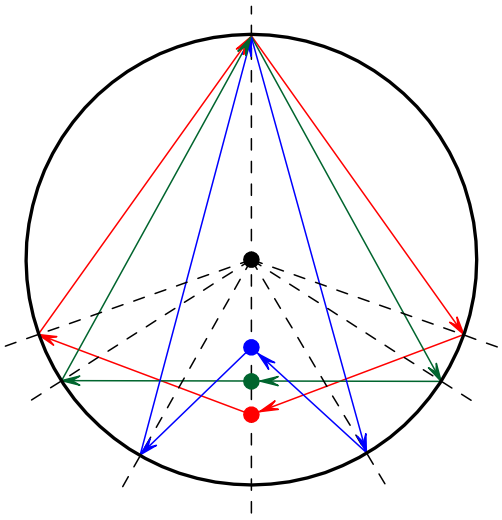

Figure 9. def $(4,1)$ electron trajectory. The triangular trajectory has the minimal length.

where Θ is the Heaviside step function and s_α is a singular point of F_α.

3.3 Large-scale inhomogeneity of the spatial distribution of electrons

Due to the electron concentration deviates from the mean value, an electric field appears in the system. The radial component of this field is denoted as $\mathcal{E}$. We evaluate $\mathcal{E}$ for the oscillating and nonoscillating parts of Δn using the expression

$$\mathcal{E}(r) = \frac{4\pi e}{r^2}\int_0^r \Delta n(r) r^2\,\mathrm{d}r\,. \tag{73}$$

At first we calculate the contribution of the rapidly oscillating part of (55) using the stationary phase method. Two cases can occur. In the first one, the function L_α has no stationary points on the integration interval, and therefore the field $\mathcal{E}$ exhibits a distinctly oscillatory behavior. Therefore, the spatial distribution of electrons has the same inhomogeneity scale, the Fermi length h/p_F.

In the second case, the function L_α has stationary points. All def (n,m)-type trajectories possess this property. An example of such trajectory def $(4,1)$ is presented in Fig. 9. To evaluate the $\mathcal{E}$ field, we apply an approximate expression of the stationary phase method,

$$\int_a^b f(x)\exp\left(\mathrm{i}\lambda s(x)\right)\mathrm{d}x \cong f(x_0)\sqrt{\frac{2\pi}{\lambda s''(x_0)}}\exp\left(\mathrm{i}\lambda s(x_0)\right), \tag{74}$$

where x_0 is an extremum point, with $s'(x_0)=0$.

We have arrived at the following expressions for the field components related to $\Delta n_{\mathrm{F,\,oscil}}$ and $\Delta n_{\mathrm{S,\,oscil}}$:

$$\Delta\mathcal{E}_{\mathrm{F,\,oscil}} = \left(\frac{18}{\pi^2}\right)^{1/3}\frac{4\pi e N^{1/3}}{r^2}\sum_\alpha \frac{F_\alpha(d_\alpha/R_0, d_\alpha/R_0)}{L_\alpha(d_\alpha/R_0, d_\alpha/R_0)} \times \frac{1}{\sqrt{L''_\alpha(d_\alpha/R_0, d_\alpha/R_0)}}\frac{s_\alpha^2}{R_0^2} \times \sin\left[\frac{1}{h}p_\mathrm{F}R_0 L_\alpha\left(\frac{d_\alpha}{R_0},\frac{d_\alpha}{R_0}\right)\right]\Theta(r-d_\alpha)\,, \tag{75}$$

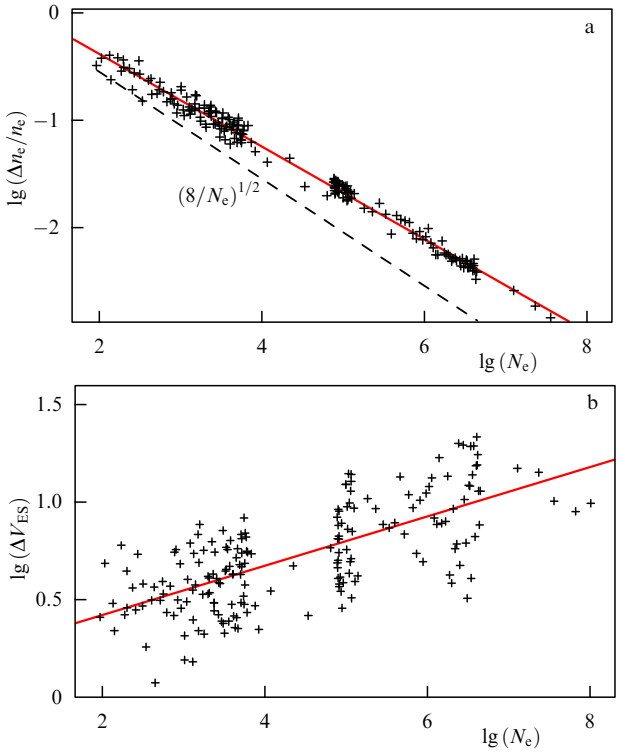

Figure 10. (a) Magnitudes of the electron density oscillations and (b) oscillations of the potential as functions of the number of electrons N_e at the same density 10^{30} m^{-3}; fitting lines for the density and potential respectively correspond to $\Delta n_\mathrm{e}/n_\mathrm{e} \propto N_\mathrm{e}^{-0.437\pm0.005}$ and $\Delta V_\mathrm{ES} \propto n^{1/3}N_\mathrm{e}^{0.142\pm0.015}$.

$$\Delta\mathcal{E}_{\mathrm{S,\,oscil}} = 3\sqrt{8}\,\frac{e\sqrt{N}}{r^2}\sum_\alpha \frac{\int_{s_\alpha/R_0}^{r/R_0} F_\alpha(x,x)x^2\,\mathrm{d}x}{L_\alpha} \times \sin\left(\frac{1}{h}p_\mathrm{F}R_0 L_\alpha\right). \tag{76}$$

Summation in (75), as well as in (76), involves all trajectories α for which $s_\alpha < r$.

The obtained expression for $\mathcal{E}(r)$ has a spatial inhomogeneity scale of the order of the spherical well size. For much greater N, $\mathcal{E}(r)$ is determined by expression (76). The structure of the sum in (76) is such that $\mathcal{E}(r)$ has extremum points s_α. For rot (n,m)-type trajectories with small n and m, we have $s_\alpha \cong R_0/4, R_0/2, \sqrt{2}R_0/2$ (see Section 3.2). Radial integration of the field $\mathcal{E}(r)$, which yields the potential, preserves the revealed periodicities as well as the large-N asymptotic behavior.

Thus, the results obtained using Green's functions (56) and (76) are in good agreement with numerical results for the behavior of the potential obtained by other methods described above (see Sections 2.1 and 2.2 and Fig. 10).

4. Inhomogeneous distribution of electrons in a compressed gas bubble: calculations using the electron density functional method

So far, we have discussed a system of free noninteracting electrons; we demonstrated that the distribution of the potential that they produce is inhomogeneous with a spatial scale of the order of the system size. In this section, we demonstrate that this effect also occurs in a system of interacting electrons, such as a pressurized bubble of ionized gas.

Numerical calculations of the spatial distribution of electrons and of the potential were done with the use of the DFT for the jellium model. Such calculations based on the jellium model had been done previously, e.g., in [20], but only for a relatively small number of electrons. In the jellium model, ions are represented as a continuous fixed distribution of positive charge. To perform calculations and analysis, it is most convenient to use a spherically symmetric distribution of ions and their potential, because it allows reducing the problem to one dimension. Here, we also use a modification of the jellium model, also called the stabilized jellium model [21–23], with a correction taking the averaged difference between jellium and point-like ions into account.

4.1 Computational method

For spherically symmetric problems, one-dimensional Kohn–Sham equations are to be solved in the jellium model [24]. Using a decomposition of the one-electron wave function (see Eqn (A.1) in the Appendix), we can write the Kohn–Sham equation for the radial wave function (to simplify the expressions, we use the atomic system of units with $\hbar = c = e = 1$):

$$\left[-\frac{1}{2}\frac{\mathrm{d}^2}{\mathrm{d}r^2} + V_{\mathrm{KS}}(r) + \frac{l(l+1)}{2r^2}\right]\chi_{nl}(r) = \varepsilon_{nl}\chi_{nl}(r)\,, \tag{77}$$

$$V_{\mathrm{KS}}(r) = V_{\mathrm{ion}}(r) + V_{\mathrm{H}}(n_{\mathrm{e}}, r) + V_{\mathrm{xc}}(n_{\mathrm{e}}, r) + \langle\delta v\rangle_{\mathrm{WS}}\big(n_{\mathrm{ion}}(r)\big)\,, \tag{78}$$

where V_{KS} is the effective Kohn–Sham potential, V_{H} and V_{ion} are the respective electrostatic potentials of electrons (Hartree potential) and of the ionic jellium multiplied the electron charge $-e$, i.e., $V_{\mathrm{H}} = -e\varphi_{\mathrm{e}} = -\varphi_{\mathrm{e}}$ and $V_{\mathrm{ion}} = -e\varphi_{\mathrm{ion}} = -\varphi_{\mathrm{ion}}$. Next, V_{xc} is an exchange-correlation potential and $\langle\delta v\rangle_{\mathrm{WS}}$ is the stabilized jellium correction. The electron density is defined in the following way:

$$n_{\mathrm{e}}(r) = 2\sum_{n,l}(2l+1)\Theta_{nl}\,\frac{\chi_{nl}^2(r)}{4\pi r^2}\,, \tag{79}$$

where $\Theta_{nl} = \Theta(E_{\mathrm{F}} - \varepsilon_{nl})$ is the Heaviside step function. The potentials and the stabilized jellium model are considered in more detail in Section 4.2 below. Hereinafter, we imply that the electrostatic potential has the form of the following sum:

$$V_{\mathrm{ES}} = V_{\mathrm{ion}} + V_{\mathrm{H}} + \langle\delta v\rangle_{\mathrm{WS}}\,. \tag{80}$$

Equations (77) are to be solved self-consistently by the method of simple iterations with mixing. At each iteration, Eqn (77) with potential (78) is solved. The new value of the electron density for the next iteration is then constructed as a combination of the one used at the current step and the one evaluated in accordance with (79). In other words, at each step of the iteration procedure, an admixture evaluated by formula (79) is added to the density. The iterations proceed until the electron density becomes self-consistent. To calculate V_{xc} in the DFT model, we every time used the exchange-correlation Perdew–Zunger potential [25] in the local density approximation (LDA) in the spin-unpolarized case.

In the case of a spherically symmetric charge distribution, the Poisson equation $\Delta\varphi = 4\pi n(r)$ can be easily integrated, and, similarly to (17), we obtain the electrostatic potential of electrons

$$V_{\mathrm{H}}(r) = \frac{1}{r}\int_0^r 4\pi\bar{r}^2 n_{\mathrm{e}}(\bar{r})\,\mathrm{d}\bar{r} + \int_r^{+\infty} 4\pi\bar{r}n_{\mathrm{e}}(\bar{r})\,\mathrm{d}\bar{r}\,. \tag{81}$$

The potential generated by the homogeneous distribution of ions V_{ion} is nothing but the potential of a uniformly charged ball.

4.2 Stabilized jellium model

There exists a correction to the Kohn–Sham effective potential $\langle\delta v\rangle_{\mathrm{WS}}$ within the stabilized jellium model. That is the averaged over the volume per ion Z/n_{ion} difference between the potential $V(r)$ of a uniformly charged ball carrying the ion charge Z and the model pseudo-potential [21–23]:

$$\langle\delta v\rangle_{\mathrm{WS}} = \frac{3}{4\pi r_0^3}\int_0^{r_0}\mathrm{d}r\,4\pi r^2\big[\omega(r) + V(r)\big]\,, \tag{82}$$

$$r_0 = Z^{1/3}r_{\mathrm{S}} = Z^{1/3}\left(\frac{3}{4\pi n_{\mathrm{ion}}}\right)^{1/3}, \tag{83}$$

where Z is the ion charge, r_{S} is the Wigner–Seitz radius, n_{ion} is the ion jellium density. $V(r)$ is the potential of a uniformly charged ball, and

$$\omega(r) = \begin{cases} -\dfrac{Z}{r}\,, & r > r_{\mathrm{c}}\,, \\ 0\,, & r < r_{\mathrm{c}} \end{cases} \tag{84}$$

is the model pseudo-potential of the interaction between an electron and a charge-Z ion; r_{c} is the characteristic radius of an 'empty' core specified by the model. Some comparisons between the stabilized jellium model and three-dimensional calculations are presented in [26].

4.3 Calculation results for homogeneous jellium

Based on the jellium model, we have performed a large number of calculations for hydrogen bubbles of various sizes and densities of ions. In this section, we consider only the case of a homogeneous density of ions, when the positive-charge density is equal to the averaged density inside the spheres, $\bar{n}_{\mathrm{e}} = N_{\mathrm{e}}(3/4\pi R_0^3)$, and is equal to zero outside.

First, let us show how the distribution of free electrons in a spherical potential well with infinitely high walls is related to that in the DFT calculation. A comparison of the result for a relatively small number of electrons is shown in Fig. 11, where, with a view to better superimpose the plots, the radius of the well is taken to be slightly larger than the ion jellium radius. The distribution of free electrons is self-similar and can therefore be simply scaled with the radius. As can be seen from the figures, the density profiles are close to each other, and the positions of maxima and minima also agree.

In the series of computations that we performed, the ion jellium density was in the range of $10^{28} - 10^{32}$ m^{-3}, and the number of electrons (equal to the number of ions) varied up to 4×10^5. In Fig. 12, we show an example of the spatial distribution of the electron density for a bubble 1 nm in radius with a jellium density of 10^{30} m^{-3} and also show the plots of the electrostatic potential and the exchange-correlation and effective Kohn–Sham potentials.

We now discuss the oscillation of the electron density and the electrostatic potential in detail. Because the ion jellium density n_{ion} is homogeneous and is approximately equal to the mean electron density n_{e}, the quantity characterizing the electron density oscillations can be conveniently chosen as the difference $n_{\mathrm{e}} - n_{\mathrm{ion}}$. We next take the magnitude Δn of

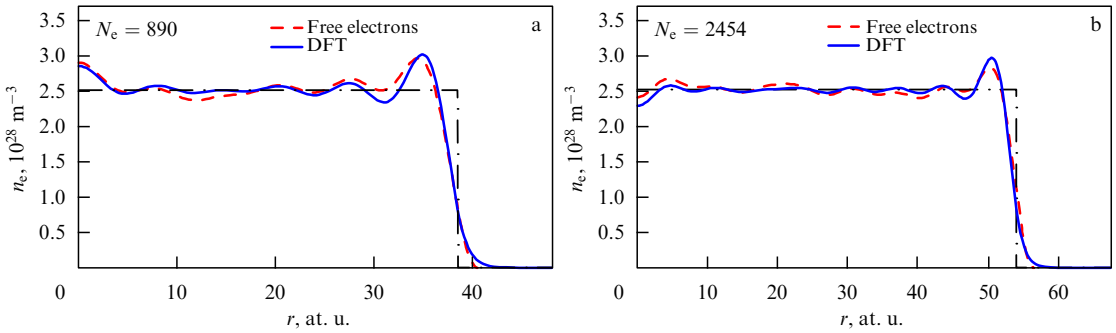

Figure 11. Electron density for free electrons (dashed line) and DFT calculation results (solid line) for (a) 890 and (b) 2454 electrons at a mean density of 2.5×10^{28} m^{-3}.

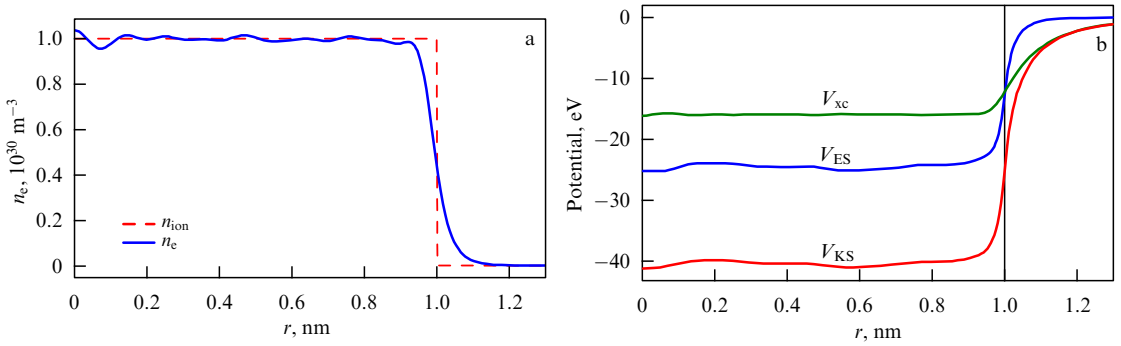

Figure 12. (a) Electron density and (b) potentials for a bubble 1 nm in radius at a mean ion jellium density of 10^{30} m^{-3} and number of electrons $N_e = 4188$.

electron density oscillations to be equal to half the difference between maximum and minimum values of $n_e - n_{ion}$ in the intermediate domain, excluding the vicinity of the boundary and the central part of the bubble, because oscillations are always very strong in the center. Oscillations in a bubble with a radius 1 nm at three different values of the ion jellium density are shown in Fig. 13. The following regularity can be discerned from the figure: the amplitudes of electron density oscillations decrease as the number of electrons increases, which is entirely consistent with the estimate in (56).

To extract the electrostatic potential oscillations ΔV_{ES}, we can, for example, subtract the mean value V_{ES}, which can be approximately expressed in terms of the Fermi energy E_F,

$$\Delta V_{ES} = V_{ES} + V_{xc}(\bar{n}_e) + \left(E_F(\bar{n}_e) - \varepsilon_{nl}^{max}\right), \qquad (85)$$

because

$$V_{ES} + V_{xc} = V_{KS} \approx -E_F\,. \qquad (86)$$

The energy of the last filled electron level ε_{nl}^{max} is subtracted here so that the values of ΔV_{ES} are in the vicinity of zero. In (85), $\bar{n}_e$ denotes the mean electron density. Examples of electrostatic potential oscillations ΔV_{ES} obtained for several bubbles with different parameters are shown in Fig. 14.

Oscillations of the electron density and potential that were obtained from numerous computations are shown in Fig. 15. Figure 15a demonstrates the magnitude of electron density oscillations depending on the number of electrons, on a logarithmic scale. We also show dependence (56) and the power-law approximation obtained by the least-square method. The fitting curve corresponds to $\Delta n_e/n_e \propto N_e^{-0.4}$.

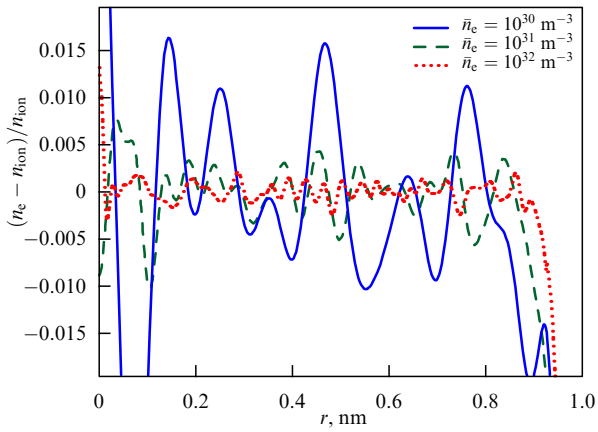

Figure 13. Electron density oscillations in a bubble 1 nm in radius at three different values of the jellium density: 10^{30}, 10^{31}, and 10^{32} m^{-3}.

From expression (76), obtained within the analytic semiclassical theory, we have

$$\varphi(r) \propto \frac{\sqrt{N_e}}{R_0} \propto n_0^{1/3} N_e^{1/6}\,. \qquad (87)$$

The potential oscillation magnitude depending on the density, which is illustrative of the semiclassical behavior, together with the dependence defined by (87) and the power-law approximation are presented in Fig. 15b. The figure does not reflect the results obtained for $N_e < 15{,}000$, because oscillations of the potential do not satisfy (87) for a relatively small number of electrons, being several times greater than

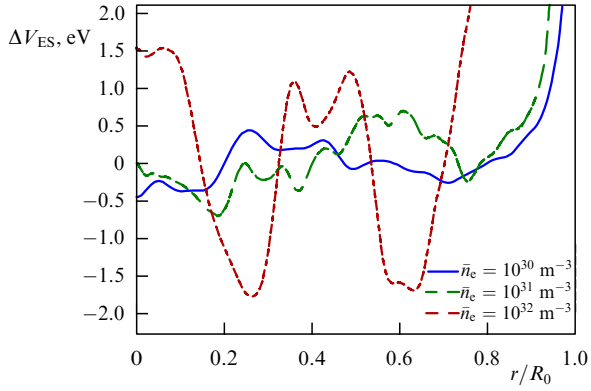

Figure 14. Electrostatic potential oscillations in bubbles with densities of 10^{30}, 10^{31}, and 10^{32} m^{-3} and with respective radii of 1.34, 1.5, and 0.5 nm.

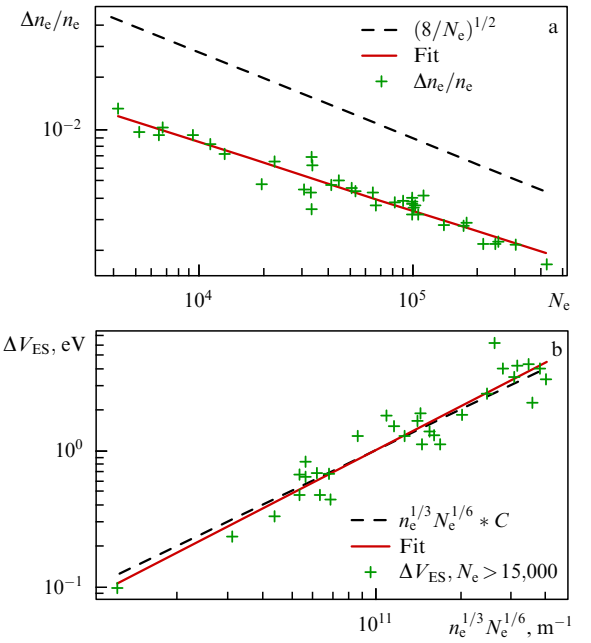

Figure 15. Dependence of (a) the electron density oscillations on the number of electrons N_e and (b) oscillations of the potential on the values of $\varphi(r)$ defined in Eqn (87), on a logarithmic scale; analytic dependences (56) and (87) obtained semiclassically are shown by dashed lines.

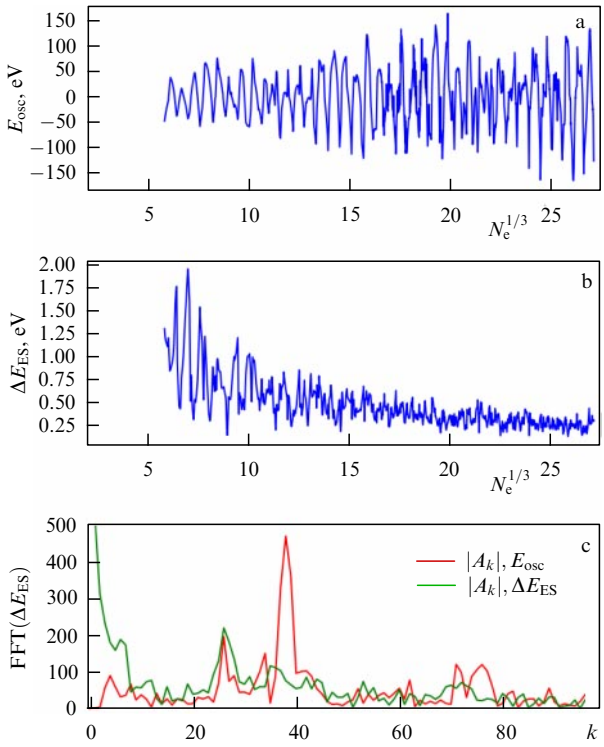

Figure 16. (a, b) Results of calculations of the oscillating part of the kinetic and electrostatic energies in the DFT model for different numbers of electrons up to $N_e = 2 \times 10^4$ (cf. [20]) and (c) fast Fourier transforms (FFTs) of these dependences.

they should be according to the power law. The fitting curve for oscillations of the potential corresponds to the dependence $\Delta V_{ES} \propto \varphi^{1.07}$, where φ is taken from (87). This correspondence means that the magnitude of oscillations of the potential is in good agreement with the analytic result.

We note the following feature of the dependence of the electrostatic potential on the number of particles in the system. Due to the factor $\sin(p_F R_0 L_\alpha/h)$ in (76), this dependence is oscillatory. In particular, there are values of N_e (magic numbers) at which the electrostatic field amplitude is maximal. This can be clearly seen from Fig. 16, which shows the results of computations of the electrostatic potential amplitude ΔV_{ES} and the oscillating part of the total energy ($E_{osc} = E - \bar{E}$) as functions of the number of electrons in the system. Computations were performed in the DFT model framework at the density $n_e = 10^{30}$ cm^{-3}. The obtained results for the oscillating part of the energy are similar to the results in [20]. The dependences are of an oscillating character with $\Delta N_e^{1/3} \approx 0.55$. By means of the Fourier transform, we can find the characteristic frequencies of such a periodic dependence. The Fourier transform was performed with respect to the argument $N_e^{1/3}$ at the interval from $N_1 = 200$ to $N_2 = 20{,}000$; the harmonic amplitudes are then given by

$$A_k = \int_{N_1^{1/3}}^{N_2^{1/3}} \exp\left(-i\omega_k N_e^{1/3}\right) f\left(N_e^{1/3}\right) \mathrm{d}N_e^{1/3}\,, \qquad \omega_k = \frac{2\pi k}{N_2^{1/3} - N_1^{1/3}}\,, \tag{88}$$

where $f(N_e^{1/3})$ is the function being sought and k is the harmonic number ranging from 0 to the number of points used in the discrete Fourier transform.

In Fig. 16c, we show the oscillating part of the energy E_{osc} and the amplitudes of the potential oscillations ΔV_{ES} as functions of the frequency number k. The frequency curve for energy exhibits several evident peaks that correspond to closed trajectories (see Fig. 5) (a similar analysis is given in [27]). For example, the peak at $k = 26$ corresponds to the simplest periodic trajectory, the motion along the diameter (see Fig. 5). The maxima at $k = 34$ and 38 correspond to the periodic trajectories of an equilateral triangle and a square. The maxima at higher k correspond to repeated periodic trajectories. Similar maxima (not necessarily well-defined) are also present on the frequency curve for the amplitude of electrostatic oscillations.

The magic numbers in the simple model of a spherical potential well were originally obtained by Gamow [6] and Elsasser [28]. They considered only small numbers of particles

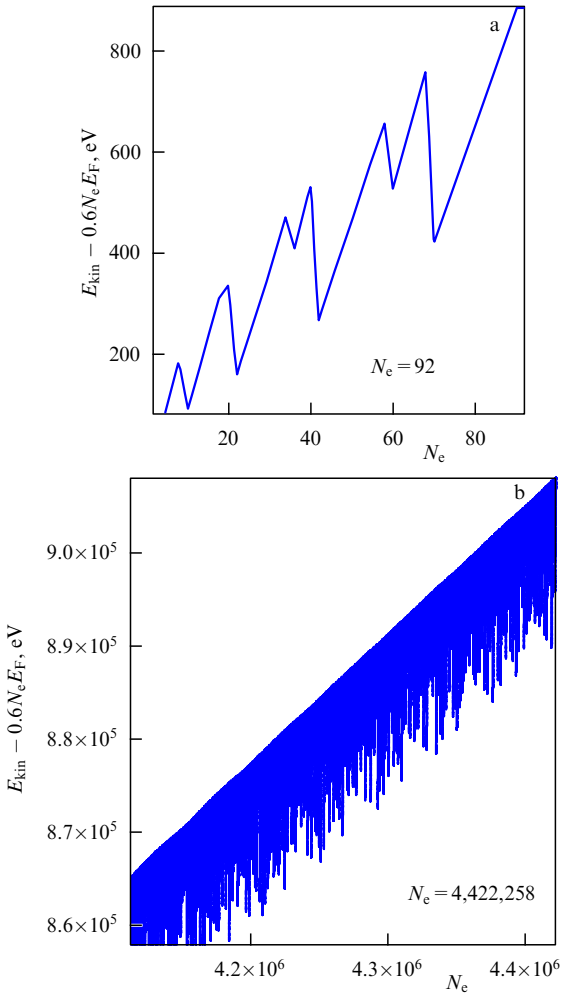

Figure 17. Kinetic energy oscillations in the simple model for (a) a small and (b) a large number of electrons.

(similarly to Fig. 17a). The simple model allows us to also observe beats in various integral characteristics of the system for a large number of particles (Fig. 17b). The differences between values of the magic numbers and those in the DFT model can be explained by differences in the behavior of the potential as r tends to the wall. The potential well has a finite depth in the DFT jellium model and is infinite in the simple model. Therefore, already at N_e of the order of a hundred, differences between the magic numbers of these models start appearing. In view of this, the 20% difference in the magic numbers that we obtain between the simplest model and the DFT is remarkably small for N_e of the order of ten thousand. In the simple model, importantly, the qualitative effect of beats can even be traced to very large N_e (Fig. 17b).

5. Conclusions

Using several methodological approaches, a new nontrivial manifestation of quantum effects in a mesoscopic system of degenerate electrons in a spherical potential well is demonstrated. We have shown that the electron density distribution has two spatial scales. The first one is the well-known Fermi length $\sim h/p_F$. We attribute a new manifestation of quantum effects to the existence of a second spatial scale, which is of the order of the system size. The second scale is most conspicuous in the emergence of an electric field acting on the ionic system. The potential has a large-scale oscillatory behavior with several extremum points.

This result was obtained for two physical systems: the gas of degenerate noninteracting electrons in a spherical potential well with infinitely high walls and a cold pressurized gas bubble of submicrometer size.

The first system was analyzed within two approaches: numerical modeling (direct numerical summation of the exact solutions for electron wave functions, numerical computation of the exact Green's function) and the analytic method of semiclassical Green's functions. The obtained results are in good agreement with each other. Numerical results confirm the main analytic dependences obtained by the method of semiclassical Green's functions.

The large-scale spatial distribution of the concentration of electrons and of the emerging electric field has several extremum points, and the amplitudes of deviations from the mean values depend on the number of electrons in the system as

$$\frac{\Delta n_e(r)}{n_e} \propto \left(\frac{8}{N_e}\right)^{1/2}, \tag{89}$$

$$\Delta\varphi \propto \frac{eN_e^{1/2}}{\varepsilon_0 R_0}. \tag{90}$$

A similar effect exists for the second system as well. DFT calculations of the pressurized gas bubble yield a similar spatial distribution of the concentration of electrons and of the electrostatic potential. In contrast to the system of free degenerate electrons, the electrons in a gas bubble interact with ions and with each other. This results in the weakening of the effect, but the functional dependences of the amplitude of deviations from the mean value exhibit a similar dependence on the number of electrons.

Of fundamental importance for the effect is the spherical symmetry of the system or its proximity to spherical symmetry. However, the effect is preserved at large deformations and under the transformation of the sphere into an ellipsoid, as was shown, e.g., in [29]. This problem was investigated in the quantum theory of elliptic billiards. Only when the deformation reaches ten percent the electron density distribution (with $N_e \sim 1000$) changes qualitatively (see, e.g., [30] and references therein). The effect is absent in flat geometry and manifests itself much more weakly in systems with cylindrical geometry [29].

The nature of this effect is different from the known manifestations of quantum effects in mesoscopic systems, such as size quantization, resonance phenomena, mesoscopic conductance fluctuations, and coherent inverse scattering.

For size quantization effects to manifest themselves, it is necessary that the system sizes be of the order of some characteristic length [31]. In particular, when a crystal sample size is comparable to the mean free path of the electron, kinetic properties such as electric conductance begin to depend on the size and shape of the crystal [32]. The effect analyzed here involves two scales: the Fermi length of the electron and the size of the domain. The ratio of these two scales has no effect on the existence of the effect or on its magnitude.

For the same reason, the effect cannot be assigned to the class of quantum resonance effects, which require that the system dimensions be equal to an integer number of half-waves (or an integer number of quarter-waves), as is the case

of resonance tunnel diodes and transistors [33], and also in the Ramsauer–Townsend effect [34].

The effect also has no interference nature, which is inherent for such phenomena as mesoscopic fluctuations of conductance and coherent inverse scattering observed in mesoscopic systems. We note that, in one of the approaches discussed in this methodological paper, concentration is determined by summing the squared moduli of the electron wave functions, which obviously eliminates any interference effects.

Our result is also essentially different from other manifestations of inhomogeneity in systems of a quantum nature: Friedel oscillations [35] and Kohn singularities [36] of the potential distribution. In those cases, the size of the inhomogeneity domain is of the order of several Fermi lengths near the boundary and is unrelated to the size and geometry of the system, with the spatial distribution of electrons being homogeneous in a major part of the system.

The nature of the phenomenon studied here is related to quantum shell effects in a spherical system. This follows from our theoretical and computational analysis, according to which the oscillatory nature of the dependence of the amplitude of the emerging large-scale electric field on the number of electrons is identical to the known dependence of the specific energy of a cluster and is determined by filled electron orbitals. The nature of the spatial distribution of the potential (the existence of several extremum points) is determined by the first few classical periodic trajectories of the electron in a spherically symmetric potential well.

Acknowledgments
The authors are grateful to Yu E Lozovik and A M Satanin for their interest in this work and their useful comments.

6. Appendix

The Schrödinger equation in the problem with potential (1) allows separation of variables, and its solution can be written as

$$u(r,\theta,\varphi)=\frac{1}{r}\,\chi_{n_r,l}(r)\,Y_{l,m}(\theta,\varphi)\,, \tag{A.1}$$

where $Y_{l,m}(\theta,\varphi)$ is a spherical harmonic. The radial wave function satisfies Eqn (3), which we reproduce here,

$$\left[\frac{\mathrm{d}^2}{\mathrm{d}r^2}-\frac{l(l+1)}{r^2}+k^2\right]\chi_{n_r,l}=0\,,\qquad k^2=\frac{2mE}{\hbar^2}\,, \tag{A.2}$$

in the interval $0\leqslant r\leqslant R_0$ and vanishes everywhere outside the interval. We here note immediately that the function $\chi(r)$ corresponds to different energy levels E depending on the orbital angular momentum l and the radial quantum number n_r, because k is to be fixed by boundary conditions. By introducing the new variable

$$x=kr \tag{A.3}$$

and replacing

$$\chi_{n_r,l}=x^{1/2}\varphi(x)\,, \tag{A.4}$$

the above equation can be brought to the form

$$\varphi''+\frac{1}{x}\,\varphi'+\left[1-\frac{(l+1/2)^2}{x^2}\right]\varphi=0\,. \tag{A.5}$$

But this is the Bessel equation. Hence, the general solution to Eqn (A.2) can be written as a combination of the linearly independent solutions

$$\chi_{n_r,l}(r)=\sqrt{\frac{\pi kr}{2}}\left[C_1J_{l+1/2}(kr)+C_2\,Y_{l+1/2}(kr)\right]. \tag{A.6}$$

Spherical Bessel functions are defined as follows:

$$j_l(x)\equiv\sqrt{\frac{\pi}{2x}}\,J_{l+1/2}(x)\,, \tag{A.7}$$

$$y_l(x)\equiv\sqrt{\frac{\pi}{2x}}\,Y_{l+1/2}(x)\,. \tag{A.8}$$

For reference, we describe the recursive calculation of $j_l(x)$.

The spherical Bessel function j_l can be expressed in terms of elementary sines and cosines:

$$j_0(x)=\frac{\sin x}{x}\,,\qquad j_1(x)=\frac{j_0(x)-\cos x}{x}\,. \tag{A.9}$$

Next, we can use the recursion relation for the general case of Bessel functions (see [37, § 17.21])

$$J_{v+1}(x)=\frac{2v\,J_v(x)}{x}-J_{v-1}(x)\,. \tag{A.10}$$

The details of the calculation of Bessel functions are discussed in Section 2.2.2. The accuracy of the calculation was compared with the new results in [14].

For the derivative of the Bessel function, we have

$$J'_v(x)=\frac{1}{2}\left\{J_{v-1}(x)-J_{v+1}(x)\right\}. \tag{A.11}$$

Using (A.11), we can eliminate J_{v-1} from (A.10),

$$J_{v+1}(x)=\frac{v\,J_v(x)}{x}-J'_v(x), \tag{A.12}$$

and obtain a recursion relation for spherical Bessel functions:

$$j_{l+1}(x)=\frac{l\,j_l(x)}{x}-j'_l(x)\,. \tag{A.13}$$

To avoid the singularity at $r=0$, we must set $C_2=0$; then, the solution for $\chi_{n_r,l}(r)$ becomes

$$\chi_{n_r,l}(r)=C_{n_r,l}\,r\,j_l(kr)\,, \tag{A.14}$$

where $C_{n_r,l}$ is a normalization constant that absorbs C_1, k, and π.

From the zero condition imposed on the wave function on the wall at $r=R_0$, we have $j_l(kR_0)=0$, whence we can find the energy levels if we find roots $x_{n_r,l}$ of the Bessel function $J_{l+1/2}(x)$:

$$J_{l+1/2}(x)=0\quad\text{ for }\quad x=x_{n_r,l}\,. \tag{A.15}$$

Here, for each orbital number l, index n_r denotes the consecutive number of a root of $J_{l+1/2}(x)$. The energy of the level n_r,l is then expressed as

$$E_{n_r,l}=\frac{\hbar^2}{2mR_0^2}\,x^2_{n_r,l}\,. \tag{A.16}$$

Hence, the root $x_{n_r,l}$ gives the dimensionless energy of the level $x^2_{n_r,l}$, and the wave number is

$$k_{n_r,l}=\frac{x_{n_r,l}}{R_0}\,. \tag{A.17}$$

The spherical harmonic $Y_{l,m}(\theta,\varphi)$ is defined as

$$Y_{l,m}(\theta,\varphi) = N_{l,m}\exp(\mathrm{i}m\varphi)P_l^m(\cos\theta)\,, \tag{A.18}$$

where $P_l^m(\cos\theta)$ is the associated Legendre polynomial, and is normalized by the condition

$$\oint \left|Y_{l,m}(\theta,\varphi)\right|^2 \mathrm{d}\Omega = 1\,, \qquad \mathrm{d}\Omega = \sin\theta\,\mathrm{d}\theta\,\mathrm{d}\varphi\,. \tag{A.19}$$

This condition is satisfied when

$$N_{l,m} = (-1)^m\left(\frac{2l+1}{4\pi}\right)^{1/2}\left(\frac{(l-m)!}{(l+m)!}\right)^{1/2}. \tag{A.20}$$

From the normalization of the full wave function $\int |u|^2\,\mathrm{d}\mathbf{x} = 1$, we then obtain

$$\int_0^{R_0}\left|\frac{1}{r}\,\chi_{n_r,l}(r)\,Y_{l,m}(\theta,\varphi)\right|^2 r^2\,\mathrm{d}r\,\mathrm{d}\Omega = 1\,, \tag{A.21}$$

whence

$$\int_0^{R_0}\left|\chi_{n_r,l}(r)\right|^2\mathrm{d}r = 1\,. \tag{A.22}$$

But, $\chi_{n_r,l}(r) = C_{n_r,l}\,r\,j_l(kr)$, whence

$$C_{n_r,l}^2\int_0^R r^2\left|j_l(kr)\right|^2\mathrm{d}r = 1\,, \tag{A.23}$$

and therefore normalizing the wave function requires calculating the integral

$$\int_0^{R_0} r^2\,\frac{\pi}{2kr}\left|J_{l+1/2}(kr)\right|^2\mathrm{d}r = \frac{\pi}{2k}\int_0^{R_0} r\left|J_{l+1/2}(kr)\right|^2\mathrm{d}r\,, \tag{A.24}$$

which must be equal to $1/C_{n_r,l}^2$. As in (A.3), we set $x = kr$, which then allows us to write

$$\frac{\pi}{2k^3}\int_0^{R_0} kr\left|J_{l+1/2}(kr)\right|^2\mathrm{d}(kr) = \frac{\pi}{2k^3}\int_0^{kR_0} x\left|J_{l+1/2}(x)\right|^2\mathrm{d}x = \frac{1}{C_{n_r,l}^2}\,. \tag{A.25}$$

The relevant integral can be evaluated as an indefinite integral (see [11], 1.8.3.11):

$$\int xJ_\nu^2(x)\,\mathrm{d}x = \frac{x^2}{2}\left(J_\nu^2(x) - J_{\nu-1}(x)J_{\nu+1}(x)\right) = \frac{x^3}{\pi}\left(j_l^2(x) - j_{l-1}(x)\,j_{l+1}(x)\right) \quad \text{for} \quad \nu = l+\frac{1}{2}\,. \tag{A.26}$$

This allows finding the normalization $C_{n_r,l}$ analytically, because the integral in (A.24) is taken for r ranging from 0 to R_0, which corresponds to $x = kR_0$ ranging from 0 to $x_{n_r,l}$:

$$C_{n_r,l}^2 = 2k_{n_r,l}^3\left[x_{n_r,l}^3\left(j_l^2(x_{n_r,l}) - j_{l-1}(x_{n_r,l})\,j_{l+1}(x_{n_r,l})\right)\right]^{-1}. \tag{A.27}$$

From (A.17) and the condition $j_l(x_{n_r,l}) = 0$, it follows that

$$C_{n_r,l}^2 = \frac{2}{R_0^3}\left[-j_{l-1}(x_{n_r,l})\,j_{l+1}(x_{n_r,l})\right]^{-1}. \tag{A.28}$$

The case $l = 0$ is not described by formula (A.28), but the integral then reduces to the elementary $\int \sin^2 x\,\mathrm{d}x$.

References

1. Kirzhnits D A, Lozovik Yu E, Shpatakovskaya G V *Sov. Phys. Usp.* **18** 649 (1975); *Usp. Fiz. Nauk* **117** 3 (1975)
2. Shpatakovskaya G V *Phys. Usp.* **55** 429 (2012); *Usp. Fiz. Nauk* **182** 457 (2012)
3. Shpatakovskaya G V *J. Exp. Theor. Phys.* **98** 455 (2004); *Zh. Eksp. Teor. Fiz.* **125** 518 (2004)
4. Kirzhnits D A, Shpatakovskaya G V *Sov. Phys. JETP* **35** 1088 (1972); *Zh. Eksp. Teor. Fiz.* **62** 2082 (1972)
5. Ekardt W *Phys. Rev. B* **29** 1558 (1984)
6. Gamow G *Nature* **131** 433 (1933)
7. Flügge S *Practical Quantum Mechanics* (New York: Springer-Verlag, 1971); Translated into Russian: *Zadachi po Kvantovoi Mekhanike* (Moscow: Nauka, 1974)
8. Messiah A *Quantum Mechanics* Vol. 1 (Amsterdam: North-Holland Publ. Co., 1961); Translated into Russian: *Kvantovaya Mekhanika* Vol. 1 (Moscow: Nauka, 1979)
9. Varshalovich D A, Moskalev A N, Khersonskii V K *Quantum Theory of Angular Momentum* (Singapore: World Scientific Publ., 1988); Translated from Russian: *Kvantovaya Teoriya Uglovogo Momenta* (Leningrad: Nauka, 1975)
10. Abramowitz M, Stegun I A (Eds) *Handbook of Mathematical Functions with Formulas, Graphs, and Mathematical Tables* (New York: Dover Publ., 1972); Translated into Russian: *Spravochnik po Spetsial'nym Funktsiyam s Formulami, Grafikami i Matematicheskimi Tablitsami* (Moscow: Nauka, 1979)
11. Prudnikov A P, Brychkov Yu A, Marichev O I *Integraly i Ryady* (Integrals and Series) Vol. 2 *Spetsial'nye Funktsii* (Special Functions) (Moscow: Nauka, 2003)
12. Baz' A I, Zel'dovich Ya B, Perelomov A P *Rasseyanie, Reaktsii i Raspady v Nerelyativistskoi Kvantovoi Mekhanike* (Scattering, Reactions and Decays in Nonrelativistic Quantum Mechanics) (Moscow: Nauka, 1971)
13. Amos D E *ACM Trans. Math. Software* **12** 265 (1986)
14. Bremer J, arXiv:1705.07820
15. Strutinskii V M, Magner A G *Sov. J. Part. Nucl.* **7** 138 (1976); *Fiz. Elem. Chastits Atom. Yadra* **7** 356 (1976)
16. Gutzwiller M C *J. Math. Phys.* **8** 1979 (1967)
17. Gutzwiller M C *J. Math. Phys.* **10** 1004 (1969)
18. Gutzwiller M C *J. Math. Phys.* **11** 1791 (1970)
19. Reichl L E *The Transition to Chaos*: *Conservative Classical Systems and Quantum Manifestations* (New York: Springer, 2004)
20. Koch E, Gunnarsson O *Phys. Rev. B* **54** 5168 (1996)
21. Perdew J P, Tran H Q, Smith E D *Phys. Rev. B* **42** 11627 (1990)
22. Perdew J P *Prog. Surf. Sci.* **48** 245 (1995)
23. Kiejna A *Prog. Surf. Sci.* **61** 85 (1999)
24. Kohn W, Sham L J *Phys. Rev.* **140** A1133 (1965)
25. Perdew J P, Zunger A *Phys. Rev. B* **23** 5048 (1981)
26. Shidlovski D S, Mukhanov A E *J. Phys. Conf. Ser.* **1009** 012012 (2018)
27. Puska M, Ogando E, Zabala N *Phys. Rev. B* **64** 033401 (2001)
28. Elsasser W M *J. Phys. Radium* **4** 549 (1933)
29. Kuratov S E, Shidlovski D S, Blinnikov S I *Phys. Plasmas* **26** 022709 (2019)
30. Kim J-H et al. *Phys. Rev. E* **96** 042205 (2017)
31. Datta S *Electronic Transport in Mesoscopic Systems* (Cambridge: Cambridge Univ. Press, 1995)
32. Li Y et al. *Nanoscale Res. Lett.* **10** 420 (2015)
33. Sun J P et al. *Proc. IEEE* **86** 641 (1998)
34. Capri A Z *Problems and Solutions in Nonrelativistic Quantum Mechanics* (River Edge, NJ: World Scientific, 2002)
35. Friedel J *Philos. Mag.* **43** 153 (1952)
36. Kohn W, Vosko S H *Phys. Rev.* **119** 912 (1960)
37. Whittaker E T, Watson G N *A Course of Modern Analysis* (Cambridge: The Univ. Press, 1927); Translated into Russian: *Kurs Sovremennogo Analiza* Pt. 1 *Osnovnye Operatsii Analiza* (Moscow: Fizmatlit, 1962)